



## WIDE FIELD CO MAPPING IN THE REGION OF IRAS 19312+1950

JUN-ICHI NAKASHIMA<sup>1</sup>, DMITRY A. LADEYSCHIKOV<sup>2</sup>, ANDREJ M. SOBOLEV<sup>2</sup>, YONG ZHANG<sup>3,4</sup>, CHIH-HAO HSIA<sup>3,4,5</sup>, AND BOSCO H. K. YUNG<sup>6</sup>

<sup>1</sup> Department of Astronomy and Geodesy, Ural Federal University, Lenin Avenue 51, 620000, Ekaterinburg, Russia; nakashima.junichi@gmail.com

<sup>2</sup> Astronomical Observatory, Ural Federal University, Lenin Avenue 51, 620000, Ekaterinburg, Russia

<sup>3</sup> Department of Physics, University of Hong Kong, Pokfulam Road, Hong Kong, China

<sup>4</sup> Laboratory for Space Research, Faculty of Science, The University of Hong Kong, Pokfulam Road, Hong Kong, China

<sup>5</sup> Space Science Institute, Macau University of Science and Technology, Avenida Wai Long, Taipa, Macau, China

<sup>6</sup> N. Copernicus Astronomical Center, Radańska 8, 87-100 Toruń, Poland

Received 2015 December 24; revised 2016 April 12; accepted 2016 April 23; published 2016 June 27

## ABSTRACT

We report the results of wide field CO mapping in the region of IRAS 19312+1950. This *Infrared Astronomical Satellite* (*IRAS*) object exhibits SiO/H<sub>2</sub>O/OH maser emission, and is embedded in a chemically rich molecular component, the origin of which is still unknown. In order to reveal the entire structure and gas mass of the surrounding molecular component for the first time, we have mapped a wide region around IRAS 19312+1950 in the <sup>12</sup>CO  $J = 1-0$ , <sup>13</sup>CO  $J = 1-0$  and C<sup>18</sup>O  $J = 1-0$  lines using the Nobeyama 45 m telescope. In conjunction with archival CO maps, we investigated a region up to 20' × 20' in size around this *IRAS* object. We calculated the CO gas mass assuming local thermal equilibrium, the stellar velocity through the interstellar medium assuming an analytic model of bow shock, and the absolute luminosity, using the latest archival data and trigonometric parallax distance. The derived gas mass (225  $M_{\odot}$ –478  $M_{\odot}$ ) of the molecular component and the relatively large luminosity ( $2.63 \times 10^4 L_{\odot}$ ) suggest that the central SiO/H<sub>2</sub>O/OH maser source is a red supergiant rather than an asymptotic giant branch (AGB) star or post-AGB star.

**Key words:** masers – stars: chemically peculiar – stars: individual (IRAS 19312+1950) – stars: jets – stars: late-type

## 1. INTRODUCTION

The isolated mid-infrared source, IRAS 19312+1950 (I19312, hereafter), exhibits SiO, H<sub>2</sub>O, and OH masers (Nakashima & Deguchi 2000, 2007; Nakashima et al. 2011). The properties of the masers of this *Infrared Astronomical Satellite* (*IRAS*) object are reminiscent of a mass-losing evolved star, such as an asymptotic giant branch (AGB) star, a post-AGB star, or a red supergiant (RSG) (Nakashima et al. 2011). For example, exhibiting SiO maser emission is a typical characteristic of AGB stars and RSGs (Genzel et al. 1980; Barvainis & Clemens 1984; Jewell et al. 1984; Nakashima et al. 2000; Imai et al. 2002b; Deguchi et al. 2004; Nakashima & Deguchi 2006; Deguchi et al. 2010; Fok et al. 2012), the bipolar molecular jet traced in the H<sub>2</sub>O maser line (Nakashima et al. 2011) is quite similar to those found in oxygen-rich AGB/post-AGB stars (Imai et al. 2002a; Yung et al. 2011), and the intensity ratio of the OH maser satellite line to the main lines (>1; Nakashima et al. 2011) is consistent with those of mass-losing evolved stars with a cold dust envelope (Habing 1996; Yung et al. 2013, 2014). The infrared properties of I19312 are also consistent with those of mass-losing evolved stars. For example, the mass-loss rate obtained by fitting dust radiative transfer models supports the AGB star status (Murakawa et al. 2007) and the near-infrared morphology is reminiscent of that of post-AGB stars and proto planetary nebulae (PPNe; Deguchi et al. 2004; Murakawa et al. 2007). In addition, Cooper et al. (2013) classified I19312 as an M-type supergiant, since the near-infrared spectrum exhibits continuum emission that peaks in the middle of the 1.5–2.5  $\mu\text{m}$  region, as well as showing molecular absorption lines suggesting a cool atmosphere and strong H<sub>2</sub>O absorption. Lumsden et al. (2013)

similarly classified I19312 as a PPN, based on the properties of infrared spectra and images.

At the same time, however, some other observational characteristics of I19312 cannot be explained in the standard scheme of stellar evolution in its late stage. For example, the gas mass estimated from a single-dish CO radio observation is 10  $M_{\odot}$ –15  $M_{\odot}$  (Nakashima et al. 2004; Nakashima & Deguchi 2005); such a large gas mass is difficult to explain as materials expelled from an AGB/post-AGB star (we give a new estimation of the gas mass in the present study; see Section 4.1). Even if we assume an RSG with a larger initial mass, the interpretation is not straightforward, because a rich set of molecular species has been detected toward I19312 (Deguchi et al. 2004), which is not typical for RSGs. So far, more than a dozen molecular species have been detected, including both carbon- and oxygen-bearing molecules (Deguchi et al. 2004). A complex chemistry including carbon-bearing molecules seems to be unusual for mass-losing evolved stars exhibiting SiO, H<sub>2</sub>O, and OH masers, because these maser molecules are usually found only in oxygen-rich chemistry. The intensity peak velocities of the radio molecular lines of carbon-bearing molecules almost exactly correspond to the systemic velocity obtained from maser observations (Deguchi et al. 2004; Nakashima et al. 2011). Interestingly, the detected molecules include CH<sub>3</sub>OH (Deguchi et al. 2004; Nakashima et al. 2015), which has not been detected so far in any other evolved stars (see, e.g., Kawaguchi et al. 1995; Chamley & Latter 1997; Cernicharo et al. 2000; He et al. 2008; Gomez et al. 2014). Furthermore, Class I methanol lines have recently been detected toward I19312 (Nakashima et al. 2015); the authors suggested that Class I methanol maser emission is emitted from an interaction region between the outflow of an RSG and ambient molecular components.

Although the possibility of I19312 being a young stellar object (YSO), which somehow exhibits SiO, H<sub>2</sub>O, and OH masers, has been considered in the past (see, e.g., Nakashima et al. 2011), the characteristics of I19312 are clearly different from such YSOs embedded in molecular clouds. For instance, I19312 shows an isolated point-like feature in mid-infrared images (see, e.g., Nakashima et al. 2011), while all YSOs with SiO masers are deeply embedded in their natal clouds and therefore the background of such YSOs is generally quite bright at mid-infrared wavelengths (e.g., Ori IRC 2, W51 IRs 2, and Sgr B2 MD5; Hasegawa et al. 1986); this is not the case for I19312. We also note that we do not see any enhancement of the number density of stars in optical/near-infrared images (i.e., DSS, Two Micron All Sky Survey (2MASS), and UKDIS) around I19312. For these reasons, I19312 most likely cannot be explained as a YSO or a star at pre-main-sequence stages.<sup>7</sup>

We note that some groups working on massive YSOs have paid attention to I19312, although no groups have provided strong evidence for classifying I19312 as a YSO (three studies mentioned below basically picked out I19312 only due to the large flux densities in its submillimeter/millimeter continuum emission). Wienen et al. (2012) surveyed NH<sub>3</sub> emission toward a flux-limited sample of submillimeter clumps detected by the APEX Telescope Large Area Survey: the GALaxy (ATLAS-GAL), which is an unbiased continuum survey of the inner Galactic disk at 870  $\mu$ m. I19312 was included in their target list and NH<sub>3</sub> (1, 1) and (2, 2) lines were detected; Deguchi et al. (2004) already reported detections of the same lines. The obtained rotational temperature (14.22 K) was consistent with that obtained in Deguchi et al. (2004) within the uncertainty (the value obtained by Deguchi et al. was 19 K). Csengeri et al. (2014) listed I19312 as one of the compact submillimeter continuum sources that were identified in the ASTLASGAL project. The measured source size was 33''  $\times$  28'' with a position angle of 121 $^\circ$ : the position angle is consistent with that of a molecular jet (108 $^\circ$ –130 $^\circ$ ; Nakashima & Deguchi 2005; Nakashima et al. 2011). Shirley et al. (2013) searched for HCO<sup>+</sup> 3–2 and N<sub>2</sub>H<sup>+</sup> 3–2 lines toward bright 1.1 mm continuum sources found by the Bolocam Galactic Plane Survey (BGPS; Aguirre et al. 2011). Both lines were detected toward I19312, and this was the first detections of these lines for this object.

So far, two hypotheses have mainly been considered for explaining I19312 (see, e.g., Nakashima et al. 2011): (1) a red nova formed by the merger of two main-sequence stars (or two stars going to the main sequence) and (2) a mass-losing evolved star, such as a post-AGB star or RSG, embedded in a small, isolated molecular cloud. However, neither of these hypotheses has yet been fully examined. One of the important viewpoints in considering the origin of I19312 is to see how the molecular gas of I19312 distributes and moves, in particular in the outermost region of the nebulosity. The real extent and total mass of the molecular gas could be an important clue to distinguish the above two possibilities, because for case (1) the total gas mass cannot go beyond the total mass of the merging stars (if we assume that additional gas does not flow into the

merging system), while for case (2) the total gas mass can be much larger than for case (1). Through mapping observations in several molecular rotational lines (Nakashima & Deguchi 2004, 2005), we revealed that the central part of the nebulosity (within 15''–20'' from the central star) involves a spherically expanding component and a molecular bipolar outflow, while the behavior of the outermost nebulosity is still unknown. Although in the past we made two mapping observations with the Berkeley–Illinois–Maryland (BIMA) array and the Nobeyama Radio Observatory (NRO) 45 m telescope (Nakashima et al. 2004; Nakashima & Deguchi 2005) in the CO rotational lines, those observations were not sufficient to reveal the entire distribution of the molecular component of I19312, because the BIMA observation resolved out the outermost nebulosity (the largest spatial frequency covered by the BIMA observation was roughly 15''–20''), and also because the mapping region of the NRO single-dish observation was too small (60''  $\times$  60'').

Thus, in order to reveal the entire structure of the molecular component of I19312, we performed wide field CO mapping in a region around I19312 using the 25-Beam Array Receiver System (BEARS) mounted on the NRO 45 m telescope. We also investigated a wide field <sup>13</sup>CO  $J = 1-0$  line image of the Boston University-Five College Radio Astronomy Observatory Galactic Ring Survey (GRS) (Jackson et al. 2006). With the combination of both the new observational and archival data, we studied a region with a size up to 20'  $\times$  20'.

## 2. OBSERVATIONS AND DATA REDUCTION

The CO mapping observations in the region of I19312 were made in the period from 2013 May 23 to June 2 using the NRO 45 m telescope (project number: CG122002). In total, 33 hr of the observing time were divided over 11 days (3 hr per day), and roughly 21 hr of the 33 hr were usable for observations; the remaining time was lost due to either mechanical problems or bad weather conditions. We observed three CO isotope lines, i.e., <sup>12</sup>CO  $J = 1-0$ , <sup>13</sup>CO  $J = 1-0$ , and C<sup>18</sup>O  $J = 1-0$ . The rest frequencies used in the analysis were taken from Lovas (1992) and the values are given in Table 1). We used BEARS, which is a double-side band (DSB) superconductor–insulator–superconductor heterodyne receiver array developed for the NRO 45 m telescope (Sunada et al. 2000). BEARS consists of 5  $\times$  5 arrays with a fixed grid spacing of 41''1 (Yamaguchi et al. 2000). The spectroscopic data were recorded by digital autocorrelators with a bandwidth of 512 MHz, 1024 frequency channels, and a frequency resolution of 500 kHz (Sorai et al. 2000). The observed CO lines were placed at the center of the 512 MHz spectral window. The system temperature ranged from 310 to 550 K, depending on the observing frequency, weather conditions, and the elevation of the telescope. The pointing accuracy was checked at the beginning and in the middle of each 3 hr observing session by observing the SiO  $\nu = 1$  and 2, and  $J = 1-0$  lines of the AGB star V1111 Oph with the High-Electron-Mobility Transistor receiver H40; the pointing accuracy was typically within 1''–2''. We adopted the chopper-wheel method, switching between a room-temperature load and the sky, for primary intensity calibrations. This corrects for atmospheric attenuation and antenna ohmic losses, and converts the intensity scale to the antenna temperature in the DSB ( $T_A^*$  (DSB)). The beam size, main beam efficiency, and aperture efficiency of the telescope were 14''7–16''0, 44%–49%, and 30%–36%, respectively, at 112 GHz (note:

<sup>7</sup> We also note that a recent result from near-infrared high-dispersion spectroscopy suggests that the <sup>13</sup>C abundance is significantly enhanced compared to the <sup>12</sup>C abundance toward the direction of the central star, and the <sup>13</sup>C/<sup>12</sup>C abundance ratio is far beyond the range of star forming regions (S. Parfenov 2016, private communication).

**Table 1**  
Summary of Observational Parameters

	$^{12}\text{CO } J = 1-0$	$^{13}\text{CO } J = 1-0$	$\text{C}^{18}\text{O } J = 1-0$
Rest Frequency <sup>a</sup> (GHz)	115.271202	110.201354	109.782176
Mapped Region	$500'' \times 500''$	$500'' \times 500''$	$250'' \times 250''$
Scan number ( <i>X</i> -direction)	3	12	5
Scan number ( <i>Y</i> -direction)	2	11	4
Velocity coverage ( $\text{km s}^{-1}$ )	$\pm 666.3$	$\pm 696.9$	$\pm 700.0$
Velocity resolution ( $\text{km s}^{-1}$ )	1.30	1.36	1.37
rms noise (K)	$2.13 \times 10^{-1}$	$6.05 \times 10^{-2}$	$9.85 \times 10^{-2}$

**Note.**

<sup>a</sup> Rest frequencies are taken from Lovas (1992).

BEARS consists of 25 arrays, and therefore the measurements of the beam size, main beam efficiency, and aperture efficiency slightly vary from array to array; we used an averaged value in our analysis).

We mapped a  $500'' \times 500''$  square region in the  $^{12}\text{CO } J = 1-0$  and  $^{13}\text{CO } J = 1-0$  lines, and a  $250'' \times 250''$  square region in the  $\text{C}^{18}\text{O } J = 1-0$  line, using the on-the-fly (OTF) mapping technique (Sawada et al. 2008). The regions were centered at the 2MASS position of I19312 ( $19^{\text{h}} 33^{\text{m}} 24.^{\text{s}} 249$ ,  $+19^{\circ} 56' 55''.65$ , J2000.0), and the sides of the squares were set along the directions of the right ascension (*X*-direction) and declination (*Y*-direction). We scanned the regions along the *X*- and *Y*-directions several times in turn, and the maps in the two scan directions were merged using the basket-weave technique (Emerson & Graeve 1988). The scan numbers in each direction, the achieved rms noise, the velocity coverages, and the velocity resolutions are summarized in Table 1. The scan speed applied was  $30'' \text{ s}^{-1}$  throughout all the observations.

In order to reduce the OTF data, we used the software package NOSTAR, which was developed for handling BEARS data from NRO. We followed the standard reduction procedure for NRO<sup>8</sup>; the standard procedure includes splitting the spectra of each spectrometer, scaling the intensity, subtracting a baseline by fitting a low-order polynomial, flagging bad channels, applying the basket-weave technique, and creating FITS cubes. We applied the Bessel–Gaussian function to convolve the maps, using a grid spacing of  $10''$ . The image processing and analysis of the reduced FITS cubes were performed using the software package Miriad (Sault et al. 1995).

In addition to the NRO data, we also used archival data of the Boston University-FCRAO GRS. GRS is a molecular line survey of the inner Galaxy using the SEQUOIA multi-pixel array receiver on the FCRAO 14 m telescope in the  $^{13}\text{CO } J = 1-0$  line (Jackson et al. 2006). The sensitivity, spectral resolution, angular resolution, and sample spacing of GRS are  $<0.4 \text{ K}$ ,  $0.2 \text{ km s}^{-1}$ ,  $46''$ , and  $22''$ , respectively. The location of I19312 is included in the two data cubes in the GRS archive<sup>9</sup> (the file names of the used data in the archive are *grs-55-cube.fits* and *grs-56-cube.fits*). The image processing and analysis of the GRS data were performed using the software package Miriad.

<sup>8</sup> See <http://www.nro.nao.ac.jp/~nro45mrt/html/obs/otf/index-e.html>.

<sup>9</sup> See <http://grunt.bu.edu/grs-stitch/download-all.php>

### 3. RESULTS

In Figures 1 and 2, we present the velocity-channel maps of the BEARS observations in the  $^{13}\text{CO } J = 1-0$  and  $^{12}\text{CO } J = 1-0$  lines. Although we observed the  $\text{C}^{18}\text{O } J = 1-0$  line as well, the velocity-channel map of this line is omitted due to its low signal-to-noise ratio. In Figures 1 and 2, we can clearly see the isolated CO emission of I19312 at the mapping center ( $34.5\text{--}38.5 \text{ km}^{-1}$  in Figure 1 and  $35.5\text{--}39.5 \text{ km}^{-1}$  in Figure 2). Using the present observations, we reveal the entire structure of the CO emission of the molecular component of I19312 for the first time. As shown in the BIMA observation (Nakashima & Deguchi 2005), the CO emission of I19312 shows a velocity gradient in the north–west to south–east directions (see the lower panel of Figure 3). The velocity gradient is also confirmed in Figure 1 (at  $34.5\text{--}38.5 \text{ km}^{-1}$ ), while in Figure 2, the gradient is not very obvious due to the low signal-to-noise ratio of the  $^{12}\text{CO } J = 1-0$  line and also due to the effect of self-absorption (see Nakashima & Deguchi 2005). In the upper panel of Figure 3, we show the velocity-integrated intensity (zero-moment) BEARS map of the  $^{13}\text{CO } J = 1-0$  line in the vicinity of I19312; the contour map is superimposed on the UKIDSS *J*, *H*, *K*-band composite color image. Comparing the upper and lower panels in Figure 3, it is evident that the angular size of the emission region seen in the BEARS map is roughly twice the size of that seen in the BIMA map; this difference in the emission region suggests that a non-negligible amount of flux was resolved out in the BIMA observation due to interferometry (Nakashima & Deguchi 2005). The angular size of the emission region seen in the BEARS map is roughly  $90''$  in the north–south direction and  $120''$  in the east–west direction; these correspond to  $5.1 \times 10^{18} \text{ cm}$  and  $6.8 \times 10^{18} \text{ cm}$ , respectively, at a distance of 3.8 kpc (Imai et al. 2011).

In Figure 3, we see that the intensity peak of the  $^{13}\text{CO } J = 1-0$  line is shifted roughly  $10''$  from that of the near-infrared emission in the north–west direction. This is due to the velocity gradient, which was already confirmed in the BIMA observation (Nakashima & Deguchi 2005). Since the intensity of the blue-shifted component is slightly larger than that of the red-shifted component, the intensity peak of the zero-moment emission is shifted to the north–west direction, in which the flux of the blue-shifted component is dominant.

The upper panel of Figure 4 shows the spatially integrated BEARS spectra of I19312 in the  $^{13}\text{CO } J = 1-0$ ,  $^{12}\text{CO } J = 1-0$ , and  $\text{C}^{18}\text{O } J = 1-0$  lines. The area of integration is a circle with a diameter of  $25''$ , which is centered at the 2MASS position of I19312. The intensity peak velocity of  $^{13}\text{CO } J = 1-0$  of I19312

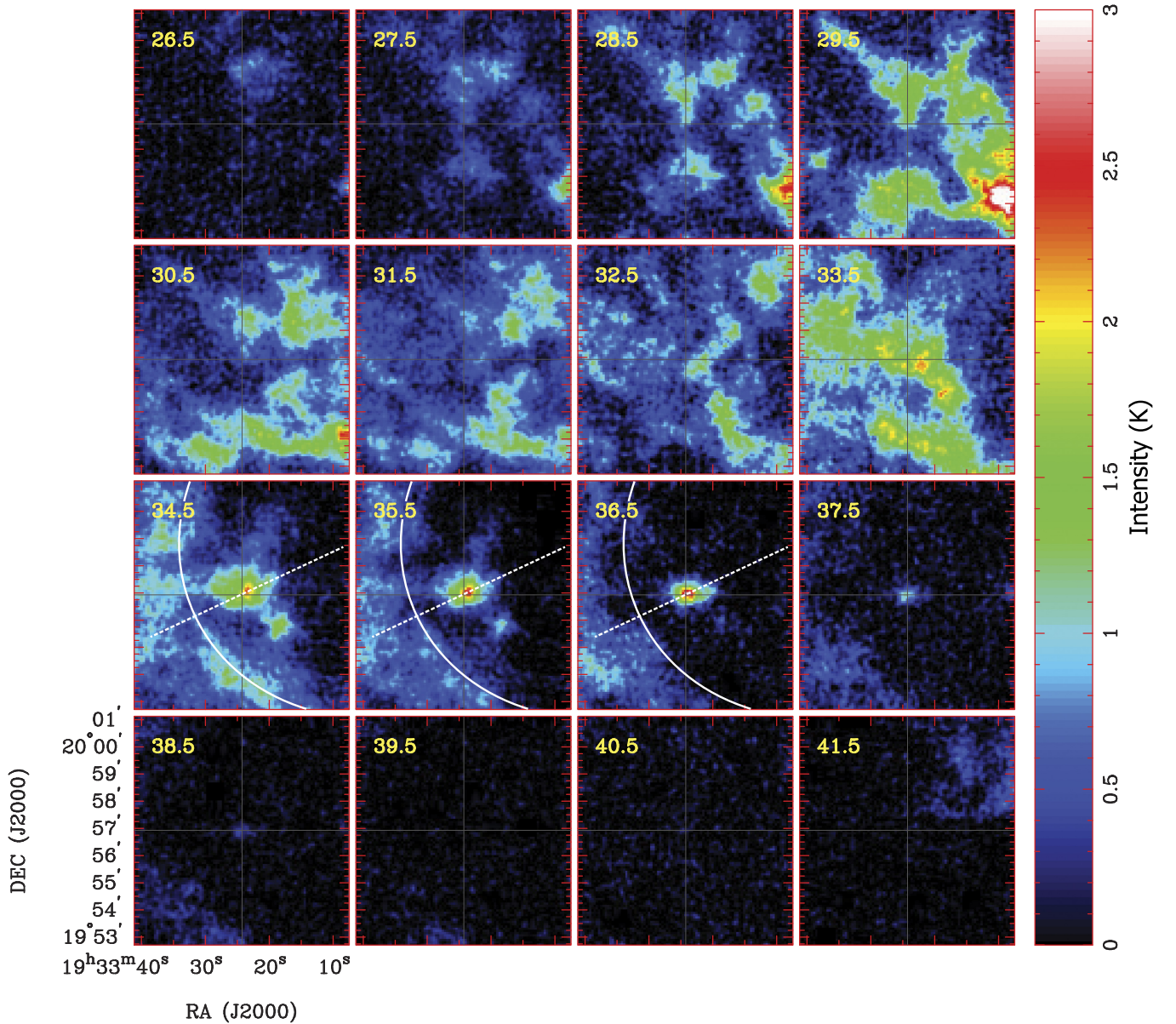
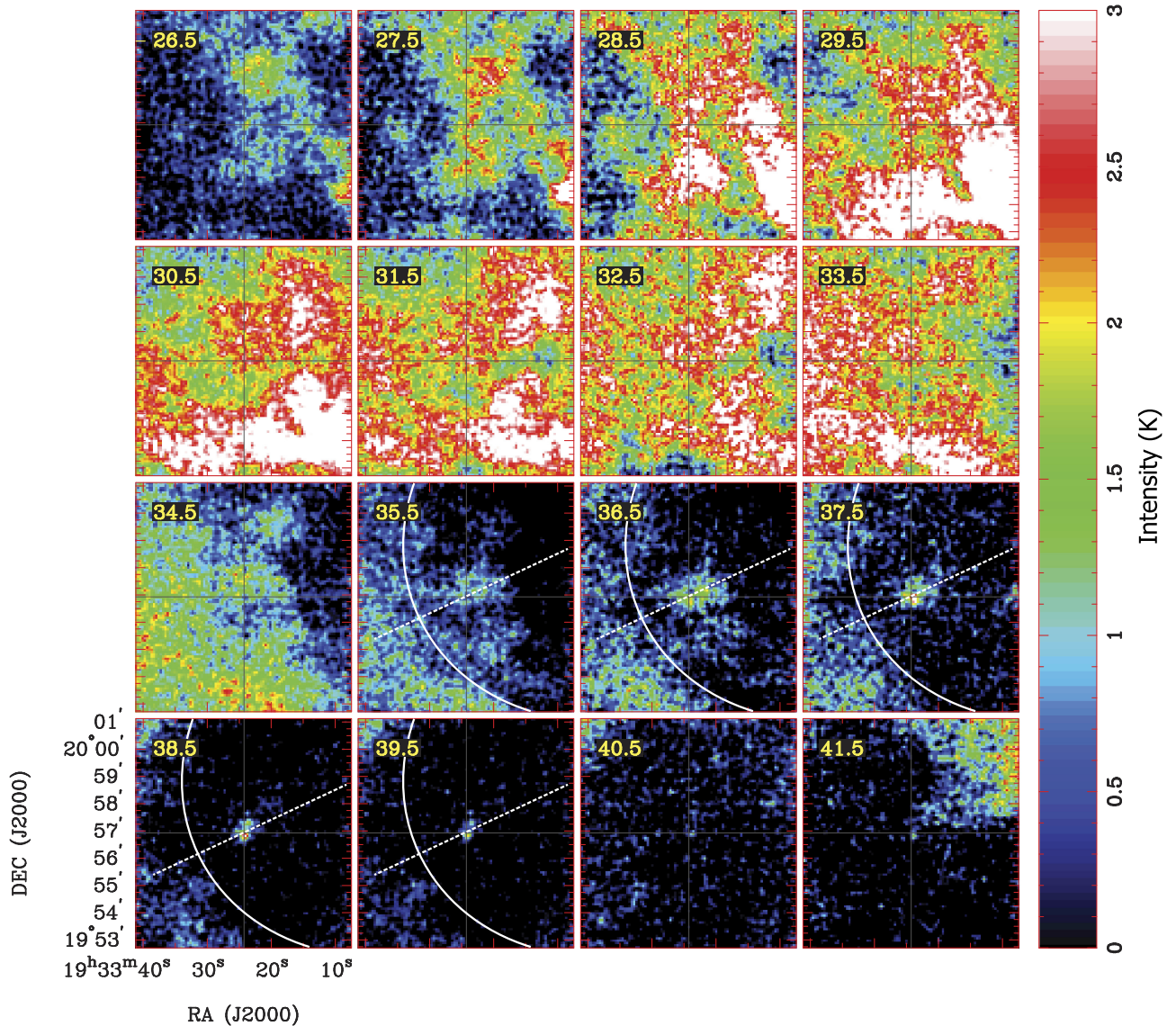


**Figure 1.** Velocity-channel maps of the  $^{13}\text{CO } J = 1-0$  line. The data were taken by the BEARS camera mounted on the NRO 45 m telescope. The radial velocity ( $V_{\text{lsr}}$ ) is given in the upper-left corner of each panel. The color intensity scale in K is given on the right side of the channel maps. The intersection of the gray vertical and horizontal lines represents the location of IRAS 19312+1950 (2MASS position). The white curve (part of an ellipse) indicates the inner boundary of a possible bow-shock feature, and the white broken line represents the long axis of the ellipse.

(at  $\sim 35 \text{ km s}^{-1}$ ) is consistent with the intensity peak velocity of other molecular lines (roughly  $35\text{--}36 \text{ km s}^{-1}$ ; see, e.g., Deguchi et al. 2004; Nakashima et al. 2004, 2015), and is also consistent with the median of the intensity peak velocities of SiO, H<sub>2</sub>O, and OH maser emission (Nakashima et al. 2011). (Note: since the SiO, H<sub>2</sub>O, and OH masers exhibit multiple intensity peaks with strong time variation in their profiles, it is difficult to obtain the precise systemic velocity of the maser source, but the median velocity of maser emission (i.e., the averaged velocity of the highest and lowest velocity components) is consistent with that of thermal lines within several  $\text{km s}^{-1}$ ). The intensity peak of the  $\text{C}^{18}\text{O } J = 1-0$  line also seems to be consistent with the velocity of other molecular lines, although it is slightly shifted ( $\sim 1 \text{ km s}^{-1}$ ) presumably due to the low signal-to-noise ratio. Although the  $^{13}\text{CO } J = 1-0$  line exhibits three intensity peaks in its spectrum

( $\sim 29.3$ ,  $\sim 35$ , and  $\sim 44.5 \text{ km s}^{-1}$ ), the  $\sim 29.3$  and  $\sim 44.5 \text{ km s}^{-1}$  components seem to be parts of an extended cloudlet which is not directly related to I19312. The  $^{12}\text{CO } J = 1-0$  line does not show the intensity peak at  $\sim 35 \text{ km s}^{-1}$ , which is the systemic velocity of the central maser source of I19312. As discussed in our previous papers (see, e.g., Nakashima et al. 2004; Nakashima & Deguchi 2005), this seems to be due to self-absorption in the  $^{12}\text{CO } J = 1-0$  line.

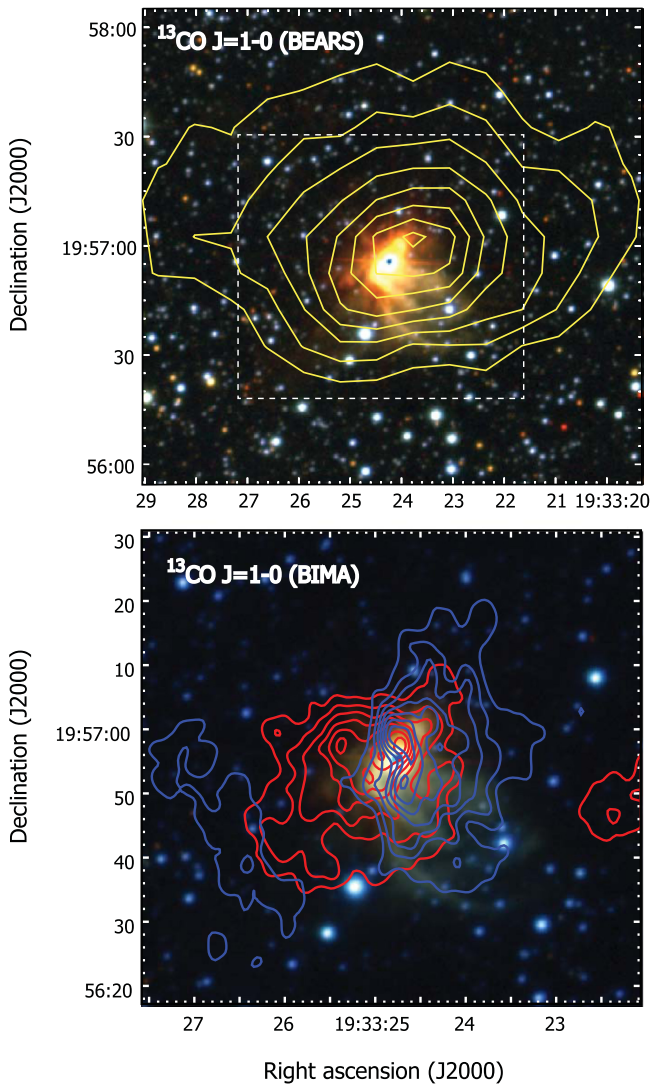
An interesting observation from Figures 1 and 2 is that we see an arc-like (or bow-shock-like) structure in the velocities from  $34.5$  to  $36.5 \text{ km s}^{-1}$  in Figure 1 and from  $35.5$  to  $39.5 \text{ km s}^{-1}$  in Figure 2, and this is reminiscent of interacting regions, which are occasionally found around mass-losing evolved stars (see, e.g., Ueta et al. 2006; Martin et al. 2007; Jorissen et al. 2011; Decin et al. 2012). In Figures 1 and 2, we indicate the crude location of the inner boundary of the arc-like structure with an



**Figure 2.** Velocity-channel maps of the  $^{12}\text{CO } J = 1-0$  line. The notations of the figure are the same as Figure 1.

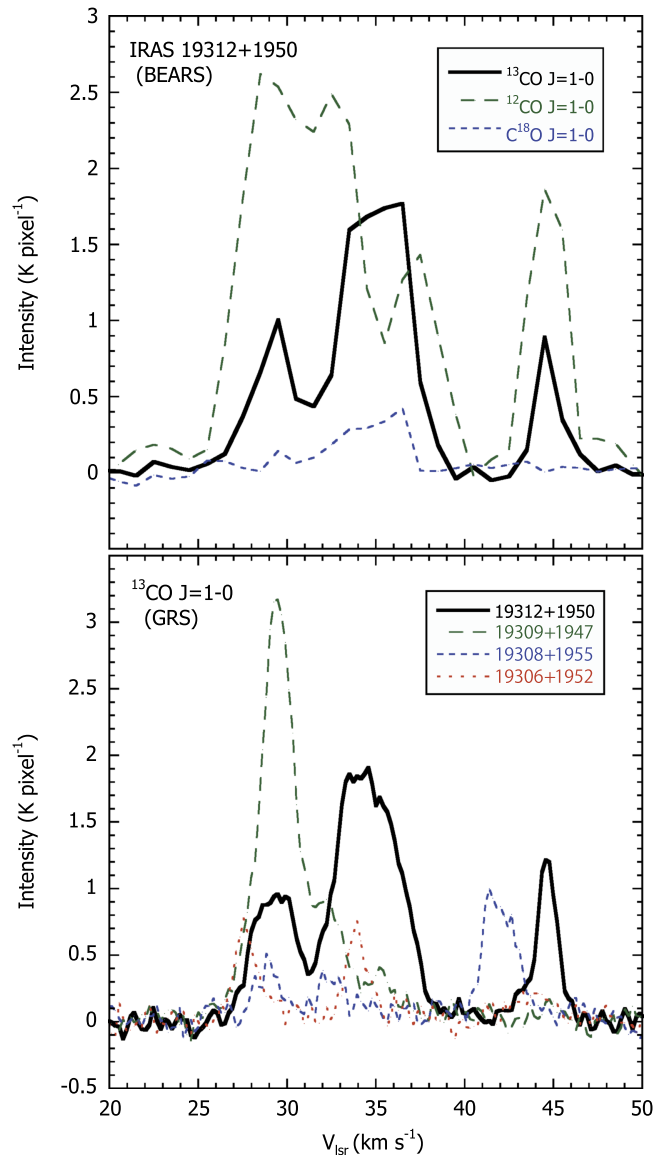
ellipse, which is fitted by eye. We note that this arc-like feature is also similarly seen in the *AKARI* far-infrared image, although the location of the *AKARI* feature is slightly different from that of the CO feature. (Kawada et al. 2007); see Figure 5. The dashed straight lines in Figures 1 and 2 represent the long axis of the fitted ellipse. Interestingly, the position angle of the long axis of the fitted ellipse ( $115^\circ$ ) is close to those of the jet axes of the  $\text{H}_2\text{O}$  maser jet ( $108^\circ$ ; Nakashima et al. 2011) and CO molecular bipolar flow ( $130^\circ$ ; Nakashima & Deguchi 2005), and it is also not greatly different from the position angle of the symmetric axis of the near-infrared structure ( $143^\circ$ ; Murakawa et al. 2007). Of course, this arc-like structure could have arisen from extrinsic circumstances due to the inhomogeneity of the ambient gas and dust. However, as a possibility, such an arc-like structure of hydrodynamical interactions can exist around a mass-losing evolved star. The detection of the Class I methanol maser line (Nakashima et al. 2015) is also suggestive of the existence of an interaction/shock region around I19312. Later, in Section 4.2, we provide some more quantitative discussion of this possible arc-like structure.

Figure 6 shows the GRS maps of the  $^{13}\text{CO } J = 1-0$  line, which covers a wider region than that of Figures 1 and 2 (the map size of Figure 6 is  $20' \times 20'$ ). We note that, even though here we present only part of the velocity coverage of the GRS data cube, almost no CO emission is detected from the velocity range of Figure 6 (the entire velocity coverage of the GRS data cube is from  $-5.0$  to  $85.0 \text{ km s}^{-1}$ ). In Figures 5 and 6, we compare CO maps, the *IRAS* point source catalog (PSC) sources, and *AKARI* far-infrared images (Kawada et al. 2007), to enable reinspection of the isolation of I19312, which is mentioned in Section 1 and our previous papers (see, e.g., Nakashima et al. 2011, 2015). Within  $10'$  from the location of I19312, seven *IRAS* PSC sources are found; the details of the nearby seven *IRAS* sources are summarized in Table 2. Although we checked the SIMBAD database for these seven *IRAS* sources, no significant information was found (except for *IRAS* measurements). In Figure 5 (*AKARI* far-infrared image), we show the locations of the nearby seven *IRAS* sources with white crosses. As seen in Figure 5, except for *IRAS* 19309 +1947, all the other six *IRAS* sources do not have a clear counterpart in the *AKARI* far-infrared image; we see only an



**Figure 3.** Upper panel: velocity-integrated intensity map of the  $^{13}\text{CO } J = 1-0$  line. The data were taken by the BEARS camera mounted on the NRO 45 m telescope. The background is a  $J$ ,  $H$ ,  $K$ -band composite color image of the UKIDSS data (for both the upper and lower panels). The velocity range for the integration is from  $34.5$  to  $39.5 \text{ km s}^{-1}$ . The contour levels start from  $2.0 \text{ K km s}^{-1}$ , and the levels are spaced every  $0.871 \text{ K km s}^{-1}$ . The highest contour corresponds to  $8.1 \text{ K km s}^{-1}$ . The white dashed square represents the size of the lower panel. Lower panel: velocity-integrated intensity map of the  $^{13}\text{CO } J = 1-0$  line. The data were taken by the BIMA array (Nakashima & Deguchi 2005). The blue contours represent the velocity ranges of  $35\text{--}36 \text{ km s}^{-1}$ , and the red contours represent the velocity ranges of  $37\text{--}38 \text{ km s}^{-1}$ . The contour levels start from  $1.0 \text{ Jy beam}^{-1}$ , and the levels are spaced every  $0.77 \text{ Jy beam}^{-1}$ .

extended cloudlet at the corresponding locations. In addition, the color of the cloudlet is significantly red in the image; this means that  $160 \mu\text{m}$  emission is distinctly dominant (note: the  $160 \mu\text{m}$  image represents the red color in the RGB color synthesis in Figure 5; the central wavelengths of the other two images used for the color synthesis are  $90 \mu\text{m}$  (green) and  $60 \mu\text{m}$  (blue)). In Figure 6 (GRS  $^{13}\text{CO}$  map), we see  $^{13}\text{CO}$  emission at the locations of IRAS 19309+1947, IRAS 19308+1955, and IRAS 19306+1952. The GRS  $^{13}\text{CO}$  spectra of these three sources are given in the lower panel in Figure 4. The CO emission of IRAS 19308+1955 and IRAS 19306+1952 is relatively weak and seems to be shapeless rather than point-like. According to these properties, the *IRAS* sources in Table 2



**Figure 4.** Upper panel: spatially integrated BEARS spectra of the  $^{13}\text{CO } J = 1-0$  (thick black line),  $^{12}\text{CO } J = 1-0$  (green dashed line), and  $\text{C}^{18}\text{O } J = 1-0$  (blue dashed line) lines toward IRAS 19312+1950. The integration region is a circle with a radius of  $25''$ , which is centered at the 2MASS position of IRAS 19312+1950. Lower panel: spatially integrated GRS spectra of the  $^{13}\text{CO } J = 1-0$  line toward IRAS 19312+1950 (thick black line), IRAS 19309+1947 (green dashed line), IRAS 19308+1955 (blue dashed line), and IRAS 19306+1952 (orange dotted line). The integration regions are circles with a radius of  $25''$ , which are centered at each *IRAS* position (for IRAS 19312+1950 and IRAS 19309+1947, the 2MASS and AKARI positions are used, respectively).

(except for IRAS 19309+1947) are, most likely, not stellar-type objects, such as YSOs and dense cores, which must exhibit much clearer enhancements in CO and infrared flux densities. Presumably, what we are recognizing here as *IRAS* sources are just the result of the inhomogeneity of interstellar gas and dust.

On the other hand, in Figure 5 we clearly see an infrared point source at a location very close to the *IRAS* position of IRAS 19309+1947. We mentioned this object in our previous study (Nakashima et al. 2004). The *IRAS* [12]–[25] color ( $1.56 - 2.5 \log F_{12}/F_{25} = 2.66$ ; here,  $F_{12}$  and  $F_{25}$  are *IRAS* 12 and  $25 \mu\text{m}$  flux densities) is typical as a YSO, but the *IRAS* [25]

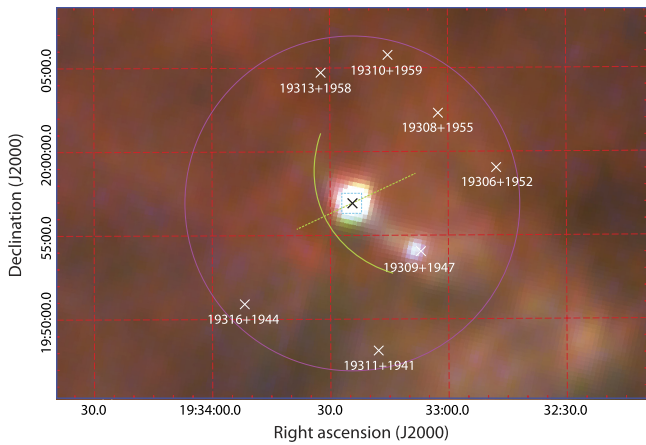


**Figure 5.** Composite color image of the AKARI far-infrared images. The AKARI N60 (60  $\mu\text{m}$ ; blue), WideS (90  $\mu\text{m}$ ; green), and N160 (160  $\mu\text{m}$ ; red) images were combined to create the false RGB color. The black cross represents the location of I19312, and the white crosses represent the locations of nearby *IRAS* sources found within 10' from I19312. The magenta circle with a radius of 10', which is centered at I19312, is given as an indicator for the angular distance from I19312. The light green curve and dashed line are the same as the white curve and dashed line given in Figures 1 and 2 (i.e., the inner boundary of a possible bow-shock feature and the axis of the structure). The blue square corresponds to the white dashed square given in the upper panel of Figure 3 (i.e., the size of the BIMA map given in the lower panel of Figure 3).

–[60] color ( $1.88 - 2.5 \log F_{25}/F_{60} = 5.32$ ; here,  $F_{25}$  and  $F_{60}$  are *IRAS* 25 and 60  $\mu\text{m}$  flux densities) is out of the YSO range due to the large 60  $\mu\text{m}$  flux (Straizys & Laugalys 2007). The search for the 6.7 GHz methanol maser emission was negative toward this object (Szymczak et al. 2000). The intensity peak velocity of this object, which is found in the lower panel in Figure 4, is shifted roughly 6  $\text{km s}^{-1}$  away from that of I19312. This velocity shift seems to be somewhat large when we compare the value with the typical velocity dispersion of a star cluster (2–3  $\text{km s}^{-1}$ ; Nakashima & Deguchi 2006; Deguchi et al. 2010). Currently, the true nature of this object is unclear, and moreover it is not clear whether this object is physically associated with I19312 or not.

#### 4. ANALYSIS

To better understand the situation, in this section we obtain the following three values: (1) CO gas mass assuming local thermodynamic equilibrium (LTE) conditions, (2) a stellar velocity against the interstellar medium assuming an analytic model of a bow shock, and (3) absolute luminosity using the latest archival photometric data and trigonometric parallax distance.

##### 4.1. CO Gas Mass Assuming LTE Conditions

One of the original purposes of the present CO observation is to reveal the entire structure of the molecular component of I19312 and to derive its total mass. Here, we estimate the CO gas mass of the isolated molecular component of I19312. In order to obtain the gas mass, we first created a map of the CO column density and then derived the mass by summing up the column densities within the emission region. The detailed procedure of the calculation is as follows.

Although we observed the  $^{13}\text{CO } J = 1-0$ ,  $^{12}\text{CO } J = 1-0$ , and  $\text{C}^{18}\text{O } J = 1-0$  lines, we finally used only the  $^{13}\text{CO } J = 1-0$  line for the mass estimation. The  $\text{C}^{18}\text{O}$  data were excluded simply

due to their low signal-to-noise ratio. The  $^{12}\text{CO } J = 1-0$  line data were tentatively processed using the following method to try to derive the excitation temperature, but we finally noticed that strong self-absorptions heavily disturbed the calculation, as given in detail later in this section, and did not use the data. In any case, in the following, we describe the details of the analysis processes for both  $^{13}\text{CO } J = 1-0$  and  $^{12}\text{CO } J = 1-0$ .

Since the beam sizes, velocity resolutions, and grid sizes of the original data cubes are different in each line, we convolved the data cubes, so that both maps have the same beam and grid sizes. The pixel numbers, grid size, velocity resolution, and beam size of the convolved data cubes are  $95 \times 101 \times 150$ ,  $5'' \times 5''$ ,  $1 \text{ km s}^{-1}$ , and  $9''.55$ , respectively. Then, we calculated the rms noise for each cube using emission free channels (specifically, we excluded velocities from 19.8 to 49.8  $\text{km s}^{-1}$  to avoid emission). The estimated rms noises are 0.33 K for  $^{12}\text{CO}$  and 0.10 K for  $^{13}\text{CO}$ .

We used the task GAUFIT in the Miriad software package (Sault et al. 1995) to fit the emission feature of the  $^{13}\text{CO } J = 1-0$  and  $^{12}\text{CO } J = 1-0$  lines in each pixel with a single Gaussian function. In this Gaussian fitting, we assumed the following three points: (1) the minimum FWHM of the line is  $1 \text{ km s}^{-1}$ , (2) the minimum line intensity is  $2\sigma$ , and (3) the central velocity of the Gaussian function is in the range from 30.5 to 38.5  $\text{km s}^{-1}$ , which corresponds to the velocity range of the CO emission of I19312.

Since the line intensity, line width, and central velocity of the line were calculated for each pixel, the output of the GAUFIT task was given as two-dimensional maps of the obtained values. Additionally, we further convolved the maps of the line intensity, line width, and the central velocity of the line with a  $10''$  Gaussian beam to avoid artificial, sudden pixel-to-pixel changes of the values.

After the Gaussian fitting, we calculated the column density distribution using the results of the Gaussian fitting. In principle, the excitation temperature ( $T_{\text{ex}}$ ) was obtained from the main beam antenna temperature ( $T_{\text{a}}$ ) of the  $^{12}\text{CO}$  line, using the solution of the radiative transfer equation (Equation 14.34 in Rohlfs & Wilson 2004). However, as stated above, in the present case it is impossible to derive the excitation temperature from the  $^{12}\text{CO } J = 1-0$  line due to the heavy self-absorption, which is lying over the systemic velocity of I19312. Thus, we assumed excitation temperatures to calculate the CO column density, so that were able to estimate the mass only from the  $^{13}\text{CO}$  line; specifically, we calculated the CO column density around ten different temperatures, which ranged from 10 K to 100 K with 10 K steps.

The optical depth of the  $^{13}\text{CO } J = 1-0$  line is obtained with the following equation (Equation 15.31 in Rohlfs & Wilson 2004)

$$\tau(^{13}\text{CO}) = -\ln \left[ 1 - \frac{T_{\text{B}}^{13}}{5.3} \left\{ \left[ \exp \left( \frac{5.3}{T_{\text{ex}}} \right) - 1 \right]^{-1} - 0.16 \right\}^{-1} \right],$$

where  $T_{\text{B}}^{13}$  is the brightness temperature of the  $^{13}\text{CO } J = 1-0$  line and  $T_{\text{ex}}$  is the excitation temperature. The source size of the compact component (90''–120'', see Section 3 for details) is larger than the beam size (15''), thus we can assume  $T_{\text{B}} = T_{\text{mb}}$ .

For linear, rigid rotor molecules such as CO or  $^{13}\text{CO}$ , with the populations of all levels characterized by a single excitation temperature  $T_{\text{ex}}$ , the column density  $N(^{13}\text{CO})$  and its optical

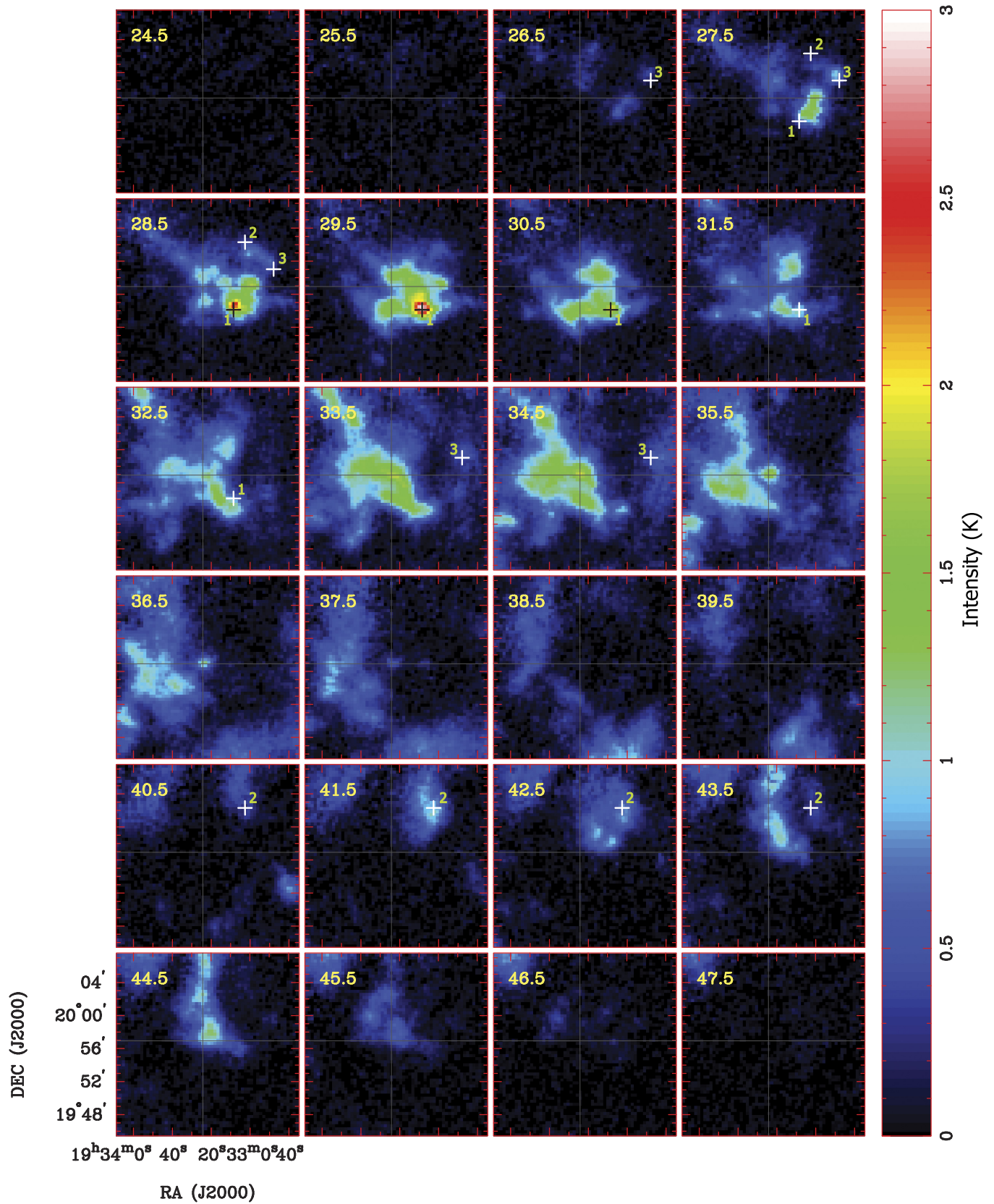


**Figure 6.** Velocity-channel maps of the  $^{13}\text{CO } J=1-0$  line. The data were taken from the GRS data archive. The crosses with identification numbers indicate the location of *IRAS* point sources within  $10'$  from IRAS 19312+1950. The identification numbers 1, 2, and 3 correspond to IRAS 19309+1947, IRAS 19308+1955, and IRAS 19306+1952. The other notations of the figure are the same as in Figure 1.

**Table 2**  
IRAS PSC sources within 10' from IRAS 19312+1950

IRAS name	$F_{12}$ (Jy)	$F_{25}$ (Jy)	$F_{60}$ (Jy)	Separation (")	CO emission (km s <sup>-1</sup> )
19306+1952	1.40	0.49	3.93	562	26.5–28.5, 33.5–34.5
19308+1955	1.00	0.59	3.93	459	27.5–28.5, 40.5–43.5
19309+1947	1.22	15.40	366.10	291	27.5–32.5
19310+1959	1.71	1.08	1.87	547	no CO emission
19311+1941	0.62	1.23	4.44	537	no CO emission
19313+1958	0.96	0.39	4.00	490	no CO emission
19316+1944	0.56	0.42	2.79	548	no CO emission

**Note.**  $F_{12}$ ,  $F_{25}$ , and  $F_{60}$  are IRAS flux densities at 12, 25, and 60  $\mu\text{m}$ .

depth  $\tau$  are related as follows (Equation (15.37) in Rohlfs & Wilson 2004)

$$N(^{13}\text{CO}) = 3.0 \times 10^{14} \frac{T_{\text{ex}}}{1 - \exp(-5.3/T_{\text{ex}})} \times \int \tau^{13}(v) dv \text{ (cm}^{-2}\text{)}.$$

In the case of a Gaussian line profile  $\int \tau^{13}(v) dv = \tau_0^{13} \sigma_v \sqrt{2\pi}$ , where  $\sigma_v$  is the velocity dispersion of the  $^{13}\text{CO}$  line and  $\tau_0$  the optical depth in the center of the line. The column density of  $\text{H}_2$  can be derived from the abundance of  $^{12}\text{CO}/^{13}\text{CO}$  and  $\text{CO}/\text{H}_2$ :

$$N(\text{H}_2) = N(^{13}\text{CO}) \times \frac{^{12}\text{CO}}{^{13}\text{CO}} \times \left[ \frac{\text{CO}}{\text{H}_2} \right]^{-1} \text{ (cm}^{-2}\text{)}.$$

In accordance with the value given in Simon et al. (2001), we adopted the value of  $\text{CO}/\text{H}_2 = 8 \times 10^{-5}$ . As mentioned in Section 1, the trigonometric parallax distance to I19312 is about 3.8 kpc (Imai et al. 2011); with this distance, the galactocentric distance of I19312 can be calculated to be 6.9 kpc. At this galactocentric distance, according to Langer & Penzias (1990), the isotope ratio,  $^{12}\text{CO}/^{13}\text{CO}$  is  $\simeq 50$ . Thus, for the calculation of the  $\text{H}_2$  column density, we used the value  $^{13}\text{CO}/\text{H}_2 = 1.6 \times 10^{-6}$ . The mass is obtained by integrating the  $\text{H}_2$  column densities over the source:

$$M = \mu m_{\text{H}_2} \int N_{\text{H}_2} dA,$$

where  $\mu$  is the ratio of the interstellar gas mass to the mass of the hydrogen molecule,  $\mu \approx 1.33$  (Hildebrand 1983),  $m_{\text{H}_2}$  is the mass of the hydrogen molecule. The surface element  $dA$  is related to the solid angle element  $d\Omega$  by  $dA = D^2 d\Omega$ . If we combine the previous three equations and constants, we can rewrite the equation for the gas mass in each pixel of the map with coordinate steps  $\Delta\alpha$  and  $\Delta\delta$ :

$$\frac{M}{M_\odot} \simeq 5.02 \times 10^{-25} D_{\text{kpc}}^2 \Delta\alpha'' \Delta\delta'' N_{\text{H}_2},$$

where  $N_{\text{H}_2}$  is the  $\text{H}_2$  column density in each pixel of the map,  $\Delta\alpha''$  and  $\Delta\delta''$  are the map step in arcseconds, and  $D_{\text{kpc}}$  is the distance to the source in kiloparsecs. We used the following values for the calculation:  $D_{\text{kpc}} = 3.8$  kpc, and  $\Delta\alpha'' = \Delta\delta'' = 5''$ . Mass is derived by summing the values from each pixel of emission.

**Table 3**  
Results of the LTE Mass Estimation

$T_{\text{ex}}$ (K)	$\tau(^{13}\text{CO})$	$N(\text{CO})$ ( $10^{16} \text{ cm}^{-2}$ )	$N(\text{H}_2)$ ( $10^{22} \text{ cm}^{-2}$ )	Mass ( $M_\odot$ )
10	0.32	1.02	0.63	225
20	0.12	1.31	0.82	290
30	0.07	1.73	1.08	382
40	0.05	2.16	1.35	478
50	0.04	2.61	1.62	576
60	0.03	3.05	1.91	674
70	0.028	3.50	2.19	773
80	0.024	3.95	2.47	872
90	0.018	4.40	2.75	971
100	0.016	4.84	3.03	1070

**Note.**  $T_{\text{ex}}$ : excitation temperatures assumed;  $\tau(^{13}\text{CO})$ : mean  $^{13}\text{CO}$  optical depths of the source;  $N(\text{CO})$  and  $N(\text{H}_2)$ : column densities of CO and  $\text{H}_2$ , respectively; Mass: derived masses.

In accordance with the CO feature found in the maps, we calculated the mass over a circle with a 40'' radius, which is centered at the 2MASS position of I19312. Consequently, at the distance of 3.8 kpc, the mass of the source (the central isolated component of I19312) is estimated to be in the range from 225 to 478  $M_\odot$ ; the range of the estimated mass corresponds to the range of the excitation temperature from <sup>10</sup> 10 to 40 K. The results of the calculation are summarized in Table 3. One may think that the derived mass in the present study is very different from those estimated in previous studies (10–15  $M_\odot$ ; see, e.g., Nakashima & Deguchi 2004, 2005). Here, we would like to note that Nakashima & Deguchi (2004) derived a gas mass using the data of a single-point observation using a single-dish telescope (i.e., they did not obtain a map), and therefore a non-negligible amount of emission of the central molecular component was missed from their observation. Note that their beam size (HPBW) was about 15'', while the integration region used in the present calculation is a circle with a 40'' radius, as we mentioned above. Therefore, the mass derived by Nakashima & Deguchi (2004) is only part of the mass derived in the present work.

#### 4.2. Stellar Velocity Assuming an Analytic Model of a Bow Shock

As mentioned in Section 3, we found a bow-shock-like structure in the velocity channels close to the systemic velocity of I19312 (see Figures 1 and 2). If we assume that this feature is a real bow shock, which is formed by hydrodynamical interaction between the interstellar medium and the stellar wind of a moving star, we can estimate the relative velocity between the interstellar medium and the star under some assumptions about the stellar wind parameters.

<sup>10</sup> Although we calculated the mass in the range from 10 to 100 K as given in Table 3, the averaged excitation temperature of the molecular component of I19312 does not seem to go beyond 40 K (presumably, much less than 40 K), because the size of the molecular component is relatively large ( $5.1\text{--}6.8 \times 10^{18}$  cm), and also because the large size seems to prevent the heating of the gas by the emission from the central star. Thus, here we give the mass corresponding to the temperature range of 10–40 K as a representative value.

**Table 4**  
Photometric Measurements of IRAS 19312+1950

Measurements (Flux Unit)	Flux Values	Reference
Optical data		
IPHAS $i'$ (mag)	18.11 ± 0.04	Barentsen et al. (2014)
Infrared Data		
2MASS $J$ (mag)	11.332 ± 0.029	Cutri et al. (2003)
2MASS $H$ (mag)	7.718 ± 0.024	Cutri et al. (2003)
2MASS $K_s^a$ (mag)	6.615	Cutri et al. (2003)
$J$ (mag)	10.7 ± 0.1	Nakashima et al. (2004)
$H$ (mag)	7.80 ± 0.1	Nakashima et al. (2004)
$K$ (mag)	6.30 ± 0.1	Nakashima et al. (2004)
WISE3.4 $\mu\text{m}$ (Jy)	4.365 ± 0.076	Cutri et al. (2012)
WISE12 $\mu\text{m}$ (Jy)	0.253 ± 0.01	Cutri et al. (2012)
WISE22 $\mu\text{m}$ (Jy)	2.122 ± 0.002	Cutri et al. (2012)
Spitzer3.6 $\mu\text{m}^b$ (Jy)	2.65 ± 0.46	This study
Spitzer4.5 $\mu\text{m}^b$ (Jy)	3.21 ± 0.58	This study
Spitzer5.8 $\mu\text{m}^b$ (Jy)	11.42 ± 1.67	This study
Spitzer8.0 $\mu\text{m}^b$ (Jy)	10.52 ± 1.33	This study
MSX 8.3 $\mu\text{m}$ (Jy)	11.84 ± 0.49	Egan et al. (2003)
MSX 12.1 $\mu\text{m}$ (Jy)	22.68 ± 1.13	Egan et al. (2003)
MSX 14.7 $\mu\text{m}$ (Jy)	23.08 ± 1.41	Egan et al. (2003)
MSX 21.3 $\mu\text{m}$ (Jy)	45.00 ± 2.70	Egan et al. (2003)
IRAS12 $\mu\text{m}$ (Jy)	22.61 ± 0.95	Moshir et al. (1992)
IRAS25 $\mu\text{m}$ (Jy)	69.77 ± 2.73	Moshir et al. (1992)
IRAS60 $\mu\text{m}$ (Jy)	317.60 ± 17.15	Moshir et al. (1992)
IRAS100 $\mu\text{m}$ (Jy)	427.00 ± 21.35	Moshir et al. (1992)
AKARI 9 $\mu\text{m}$ (Jy)	13.71 ± 0.14	Ishihara et al. (2010)
AKARI 18 $\mu\text{m}$ (Jy)	37.02 ± 0.45	Ishihara et al. (2010)
AKARI 65 $\mu\text{m}$ (Jy)	313.10 ± 29.40	Ishihara et al. (2010)
AKARI 90 $\mu\text{m}$ (Jy)	176.30 ± 38.90	Ishihara et al. (2010)
AKARI 140 $\mu\text{m}$ (Jy)	302.90 ± 42.00	Ishihara et al. (2010)
AKARI 160 $\mu\text{m}$ (Jy)	275.10 ± 31.80	Ishihara et al. (2010)
IRAS IGA 60 $\mu\text{m}$ (Jy)	379.62 ± 0.68	Mottram et al. (2010)
Spitzer MIPS 70 $\mu\text{m}$ (Jy)	556.13 ± 3.07	Mottram et al. (2010)
IRAS IGA 100 $\mu\text{m}$ (Jy)	303.13 ± 6.55	Mottram et al. (2010)
ATLASGAL 870 $\mu\text{m}$ (Jy)	2.79	Csengeri et al. (2014)
ATLASGAL F 870 $\mu\text{m}$ (Jy)	2.45	Wienen et al. (2012)
BGPS 1100 $\mu\text{m}$ (Jy)	1.18 ± 0.16	Dunham et al. (2011)
BGPS 1100 $\mu\text{m}$ (Jy)	1.186 ± 0.21	Rosolowsky et al. (2010)
Radio Data		
Planck 857 GHz (mJy)	98525 ± 8330.75	Planck Collaboration XXVIII (2014)
Planck 143 GHz (mJy)	802.97 ± 132.53	Planck Collaboration XXVIII (2014)
RMS 5 GHz <sup>c</sup> (mJy)	0.7	Cooper et al. (2013)

#### Notes.

<sup>a</sup> Note that the 2MASS  $K_s$  band flux is unreliable.

<sup>b</sup> Measured from *Spitzer* GLIMPSE images.

<sup>c</sup> Note that the flux measured from 5 GHz is an upper limit.

Assuming that the physical thickness of the shock shell is negligible and the ram pressure of the interstellar medium is balanced by that of the stellar wind, Wilkin (1996) derived an

analytic solution for bow shock, which predicts that the distance between the apex and the central star ( $R_0$ ) is given by the following formula.

$$R_0 = \sqrt{\dot{M}v_w / (4\pi\rho_{\text{ISM}}v_*^2)}$$

Here,  $\dot{M}$  is the mass-loss rate,  $v_w$  is the velocity of the stellar wind,  $\rho_{\text{ISM}}$  is the mass density of the ISM, and  $v_*$  is the velocity of the star with respect to the interstellar medium. The shape of the bow shock can be expressed by the following formula.

$$R(\theta) = R_0 \sin^{-1}\theta \sqrt{3(1 - \theta \cot\theta)}.$$

Here,  $\theta$  is the polar angle from the symmetric axis as seen from the central star at the coordinate origin. Based on the present CO observations, we derive an angular separation between the apex of the bow and the star of 125". If we assume that the distance to this object is 3.8 kpc (Imai et al. 2011) and the symmetry axis of the bow shock lies in the sky plane, we obtain  $R_0 = 7.1 \times 10^{18}$  cm. Assuming a low density atomic interstellar medium ( $n_{\text{ISM}} = 0.1 \text{ cm}^{-3}$ ) and values for  $\dot{M}$  and  $v_w$  ( $10^{-4} M_{\odot} \text{ yr}^{-1}$  and  $25 \text{ km s}^{-1}$ , respectively; Nakashima et al. 2004; Nakashima & Deguchi 2005), we derive a stellar velocity of  $11 \text{ km s}^{-1}$ .

The linear size  $R_0 = 7.1 \times 10^{18}$  cm corresponds to a distance of roughly 2.3 pc. This seems to be a relatively large distance, because it takes about  $9.0 \times 10^4$  years for matter ejected from a star to reach such a distance (assuming the expansion velocity is  $25 \text{ km s}^{-1}$ ) and the total mass ejected during this time (assuming a constant mass-loss rate  $10^{-4 \sim -5} M_{\odot} \text{ yr}$ ) would be  $90 M_{\odot}$ . For comparison, the distance is much larger than the estimated distance to bow shock in AGB stars, which is only about 0.08 pc in the case of R Hya (Ueta et al. 2006) and about 0.3 pc in Betelgeuse (Decin et al. 2012). We note that a remnant of an AGB wind, the size of which is about 1.3 pc, has been detected toward the planetary nebula NGC 7293 (Zhang et al. 2012). Based on this size, it is not particularly unnatural for hydrodynamical interactions to occur 1–2 pc away from the central star. If the central star of I19312 is/was a RSG as we discuss in Section 5, the mass-loss rate and the size of the remnant stellar wind could be more immense.

#### 4.3. Absolute Luminosity

Previously, we have given a couple of estimations about the absolute luminosity of I19312 (Nakashima et al. 2004, 2011). However, the recent results of the trigonometric parallax measurement using the VLBI technique (Imai et al. 2011) enable us to estimate a much more reliable value of the absolute luminosity, and furthermore many new photometric data have been released to the public. We carefully collected all the photometric measurements of I19312 available to the public, and recalculated the absolute luminosity of I19312 using the most reliable distance information.

In order to construct the spectral energy distribution (SED) of I19312, we used the photometric data of the following observations, surveys, and archives: the optical INT/WFC Photometric H $\alpha$  Survey of the Northern Galactic Plane (IPHAS)  $i'$ -band magnitude; 2MASS; near-infrared photometry of the  $J$ ,  $H$ ,  $K$ , and  $K_s$  bands from ground-based observation (Nakashima et al. 2004); mid-infrared images of the object extracted from the *Spitzer* Galactic Legacy Infrared Mid-Plane Survey Extraordinaire (GLIMPSE); the *Wide-Field Infrared Survey Explorer* (WISE); the *IRAS* Sky Survey; the Midcourse Space Experiment (MSX);

the Multiband Imaging Photometer of *Spitzer* (MIPS); and the AKARI IRC Survey. Many of the photometric data were obtained from the Data Discovery Service of the NASA/IPAC Infrared Science Archive.<sup>11</sup> The *Spitzer*/GLIMPSE fluxes were measured using the method described in Zhang et al. (2012) and Hsia & Zhang (2014). We used photometric data in the wavelength range between 0.763 and 2.096 mm (in total, 38 data points including upper limits). The photometric measurements collected are summarized in Table 4, and the SED diagram is given in Figure 7.

The optical–infrared photometric measurements are corrected based on two interstellar extinction coefficients toward I19312, i.e.,  $A(V) = 16.3$  (Frerking et al. 1982) and  $A(V) = 30.98$  (Schlafly & Finkbeiner 2011). The extinction coefficients  $A(V)$  were converted to  $A(J)$  using the conversion factor given by Stead & Hoare (2009). Then,  $A(\lambda)$  of corresponding wavelengths were derived based on Table 1 in Mathis (1990); we obtained the  $A(\lambda)$  value by interpolating the values in Mathis (1990) when the conversion factor was not found at the corresponding wavelength (the correction does not change the values at wavelengths longer than roughly  $4 \mu\text{m}$ ).

The emerging flux of I19312 with extinction corrections is fitted by a three-component model using the same expression as described in Hsia et al. (2010). As seen in Figure 6, only the shortest wavelength component (less than roughly  $\lambda = 5 \mu\text{m}$ ) is affected by the interstellar extinction correction. Since we have three cases of extinction corrections (i.e.,  $A(V) = 30.98$ , 16.3, and 0), three temperatures of the fitted blackbodies corresponding to each  $A(V)$  value are obtained, i.e.,  $13,000 \pm 4800 \text{ K}$  ( $A(V) = 30.98$ ),  $2100 \pm 700 \text{ K}$  ( $A(V) = 16.3$ ), and  $1100 \pm 400 \text{ K}$  ( $A(V) = 0$ ). The first result (13,000 K) clearly seems to be too high to be the temperature of a stellar maser source. This presumably means that the large extinction coefficient ( $A(V) = 30.98$ ) is not reliable. The dust component is roughly fitted by two blackbodies with temperatures of 191 and 47 K. With an assumed distance of 3.8 kpc (Imai et al. 2011), we derived the total luminosity by integrating the region under the three blackbody models. The derived total luminosities are  $2.06 \times 10^4 L_{\odot}$  ( $A(V) = 0$ ),  $2.63 \times 10^4 L_{\odot}$  ( $A(V) = 16.3$ ), and  $1.54 \times 10^6 L_{\odot}$  ( $A(V) = 30.98$ ). For the reason mentioned above, the absolute luminosity must presumably be close to  $2.63 \times 10^4 L_{\odot}$ . In fact, this value is close to those given in other studies, i.e.,  $9.6 \times 10^3 L_{\odot}$  at 3.1 kpc (Cooper et al. 2013) and  $1.37 \times 10^4 L_{\odot}$  at 3.7 kpc (Lumsden et al. 2013).

## 5. DISCUSSION

As mentioned in Section 1, the primary purpose of the present research is to reveal the entire structure and mass of the molecular component of I19312 to constrain the possibilities of the origin of this complex system, which consists of a stellar maser source and a chemically rich molecular component. With our observations, we revealed the entire structure of the molecular component of I19312, and we estimated the CO gas mass of the molecular component. In this section, we interpret the observational results given in Section 3 based on the analysis given in Section 4.

### 5.1. AGB/Post-AGB Stars and RSGs

As given in Section 4, the gas mass estimated in the present study ranges roughly from  $225$  to  $478 M_{\odot}$  (corresponding to the range of the excitation temperature from 10 to 40 K). Since we assumed LTE and optically thin conditions for the  $^{13}\text{CO}$

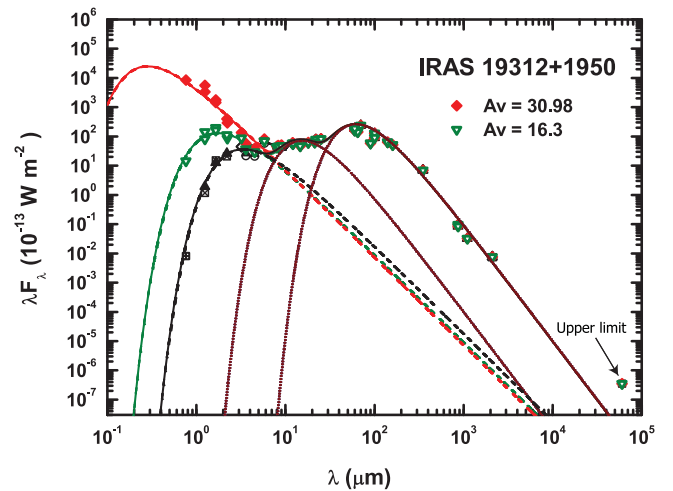


**Figure 7.** SED diagram of I19312 with extinction corrections in the wavelength range from  $0.1 \mu\text{m}$  to  $10 \text{ cm}$ . The crossed square, crossed diamonds, filled triangles, open diamonds, and half-filled circles correspond, respectively, to the data of IPHAS  $i'$ -band photometry,  $J$ ,  $H$ , and  $K$  near-infrared photometry, and the 2MASS, *WISE*, and *Spitzer* GLIMPSE surveys (although some of them may be indistinguishable due to overlap with other symbols). The green open triangles and red filled diamonds, respectively, represent the photometric data corrected using the extinction values of  $A(V) = 16.3$  and  $A(V) = 30.98$ . The blackbody curves are fitted to the emission from the photosphere (red, green, and black lines) and two dust components (brown lines). The red, green, and black lines represent the differences of the interstellar extinction corrections, i.e.,  $A(V) = 30.98$  (red),  $A(V) = 16.3$  (green), and  $A(V) = 0$  (black).

$J = 1-0$  line, the estimated gas mass should be considered as the lower limit.

Our original question in this research was whether the mass of the molecular component could be explained as materials expelled from a star (or a binary system consisting of stars). Although the bipolar molecular jet and extended infrared nebulosity of I19312 are reminiscent of those found in post-AGB stars and PPNe, which are the descendants of AGB stars, the large gas mass far beyond  $200 M_{\odot}$  cannot be interpreted as materials expelled from a single AGB star, because the main-sequence mass of an AGB star ranges roughly from  $0.8 M_{\odot}$  to  $8.0 M_{\odot}$  (see, e.g., Habing 1996; Busso et al. 1999). Even if assuming a binary system consisting of 2–3 AGB stars, it is still impossible to explain such a large mass. Thus, with the large estimated gas mass, first we can safely conclude that the molecular component of I19312 does not originate in a single AGB star (or even a binary system consisting of 2–3 AGB stars). If the central SiO/H<sub>2</sub>O/OH maser source originated in an AGB/post-AGB star, the surrounding molecular component must have been pre-existing rather than being materials expelled from the central star. If this is the case, the situation would be explained by a central AGB/post-AGB star coexisting in a small isolated cloudlet with a mass of  $225 M_{\odot}$ – $478 M_{\odot}$ , with the star and the cloudlet sharing almost the same radial velocity of about  $35 \text{ km s}^{-1}$ . However, since the age of an AGB star is typically several Gyr (see, e.g., Olszewski et al. 1996; Guarnieri et al. 1997; Maciel et al. 2011), presumably it is impossible to consider that the natal molecular gas still remains in the vicinity of the star over such a long timescale. Therefore, if the central star is really an AGB/post-AGB star, we have to consider that the coexisting situation between the star and surrounding gas is a product of “pure chance.”

Another major possibility to explain a mass-losing evolved star must be an RSG. The observational properties of RSGs are, in many aspects, quite similar to those of AGB stars. For example, the infrared colors of RSGs are basically the same as

<sup>11</sup> <http://irsa.ipac.caltech.edu/cgi-bin/Radar/nph-estimation>

those of AGB stars, because the dust temperature is almost the same (see, e.g., Fok et al. 2012). RSGs exhibit a circumstellar envelope, which is often similar to that found in AGB/post-AGB stars in nature (see, e.g., Shinnaga et al. 2003). The maser properties of RSGs are also similar to those of AGB stars, although the velocity ranges of maser emission of RSGs are somewhat larger than those of AGB stars (Nakashima & Deguchi 2007; Deguchi et al. 2010; Fok et al. 2012). However, an important difference between RSGs and AGB/post-AGB stars is their initial mass. An RSG has a larger initial mass than an AGB star; its mass-range is roughly from  $10 M_{\odot}$  to  $25 M_{\odot}$  (Levesque 2009). Therefore, the ages of RSGs are much shorter than AGB stars, say,  $<20$  million years (see, e.g., Davies et al. 2007, 2008). Even if we assume an initial mass of  $10 M_{\odot}$ – $25 M_{\odot}$ , however, all the mass of the molecular component ( $225$ – $478 M_{\odot}$ ) cannot be explained as material expelled from an RSG or a binary system including 2–3 RSGs (putting aside whether such a binary system is physically possible), as was the case for AGB/post-AGB stars. Therefore, the molecular component, in any case, must be pre-existing even if we assume an RSG. However, since the ages of RSGs are much younger than AGB stars, the surrounding materials could be still a natal cloud (or the remnant of a natal cloud) for the central RSG. In fact, in some open clusters containing RSGs still possess a molecular component, which could be natal clouds of RSGs (Deguchi et al. 2010). In such a case, however, presumably there should be a concentration of stars which are formed in the same natal cloud, but no such concentration of stars has been found so far around I19312. (Note: in a high-resolution *HST*/WFC image, we find a weak concentration of several stars in the vicinity of a red star (within roughly  $3.5''$ ), which seems to be the source of SiO/H<sub>2</sub>O/OH masers. But, it is not clear whether these stars have a physical relation to the central maser source.) In terms of the luminosity, the value derived in Section 4.3 ( $2.63 \times 10^4 L_{\odot}$ ) is consistent with the case of an RSG (Wood et al. 1983; Groenewegen et al. 2009; Fok et al. 2012), but it is not very inconsistent with the upper limit of post-AGB stars (Reyniers & Van Winckel 2001; Whitelock & Marang 2001; van Winckel 2003). For these reasons, currently, an RSG embedded in the (remnant of) a natal cloud seems to be the preferable interpretation for I19312 compared to the case of AGB/post-AGB stars lying in a small molecular component by pure chance, although all the observational properties are yet to be consistently explained.

### 5.2. Other Possibilities and Related Issues

In terms of the large mass of the molecular component, one may think that mass loss from a very massive star with an initial mass of  $100 M_{\odot}$ – $200 M_{\odot}$  could form a surrounding molecular component with a mass nearly equivalent to the stellar mass. In fact, a dozen stars with a quite large initial masses of more than  $100 M_{\odot}$  are known in the sky: for example, R136a1, R136a2, R136a3, NGC 3603-B, R136c, NGC 3603-C (Crowther et al. 2010), HD 269810 (Walborn et al. 1995), VFTS 682 (Vink et al. 2012), and WR42e (Gvaramadze et al. 2013). However, the situation of such extreme massive stars seems to be very different from the case of I19312. Most importantly, such very massive stars definitely exhibit high-energy phenomena, such as X-ray emission and extremely high outflow-velocity, due to their large self-gravity (see, e.g., Seward et al. 1979; Damiani Neto et al. 1993; Townsley et al. 2006) developing an ionized region around the

star (see, e.g., Okamoto et al. 2003; Jamet et al. 2004). This is not the case for I19312: an ionized region has not been detected so far, for example, in B $\gamma$  imaging and free-free emission surveys (Nakashima et al. 2004, 2011).

In our previous papers, we discussed the possibility of a merger of two main-sequence stars (or two stars going to the main sequence) to explain the situation of I19312 (see, e.g., Nakashima et al. 2011). Specifically, we pointed out some similarities between I19312 and V838 Mon (Nakashima et al. 2011), i.e., V838 Mon exhibits both SiO masers and extended nebulosity detected in the CO radio lines, as does I19312 (Deguchi et al. 2005; Kaminski et al. 2007; Kaminski 2008). Therefore, the most promising model explaining the observational properties of V838 Mon seems to be the merger of two stars (see, e.g., Soker & Tylenda 2007). However, the present results suggest that the surrounding gas of I19312 (roughly  $225$ – $478 M_{\odot}$ ) is much larger than that of V838 Mon (a few tens of solar masses, Kaminski 2008), and such a large mass cannot be explained by the gas expelled from two merging stars. Even in such a case, we still could assume that the SiO maser emission of I19312 is caused by the merger of two stars, like for V838 Mon, but to verify the merger presumably we should see a dense stellar concentration around the merging stars, otherwise the two stars have no chance (or a very small chance) of meeting and merging. In fact, Afşar & Bond (2007) found that V838 Mon is a member of a B-star association and the narrow CO emission can be attributed to an interstellar medium within the cluster. However, such a clear star association has not been found in the vicinity of I19312 so far, as briefly mentioned in Section 5.1.

As we discussed in Section 5.1, if the molecular component of I19312 is part of the natal cloud of an RSG with masers, another concern would be which portion of the CO emission found in Figures 1, 2, and 6 is from the same natal cloud that formed the RSG. As we calculated in Section 4.2, if we assume that the arc-like feature seen in Figures 1 and 2 is caused by a bow shock, the relative velocity is calculated to be  $11 \text{ km s}^{-1}$ . This relative velocity seems to be too large to be the velocity dispersion of a single natal cloud which formed RSGs. In fact, the velocity dispersions of open clusters including RSGs are, at most, roughly  $\sim 5 \text{ km s}^{-1}$  (typically,  $2$ – $3 \text{ km s}^{-1}$ ; Nakashima & Deguchi 2006; Deguchi et al. 2010). Therefore, if we believe that the bow shock is real, the molecular gas lying in the south-east of I19312 is probably not directly related to the formation of the RSG in I19312.

## 6. SUMMARY

We have reported the results of a wide field CO mapping in the region of I19312. We revealed the entire structure of the molecular component of I19312 for the first time. We calculated the CO gas mass assuming LTE conditions, a stellar velocity against the interstellar medium assuming an analytic model of a bow shock, and absolute luminosity using the latest archival photometric data and trigonometric parallax distance. The derived large gas mass and relatively large luminosity suggest that the central SiO/H<sub>2</sub>O/OH maser source seems to be an RSG rather than an AGB/post-AGB star, and the surrounding molecular component could be the natal cloud of the RSG.

This work is supported by Act 211 Government of the Russian Federation, agreement No. 02.A03.21.0006. Y.Z.

thanks the Hong Kong General Research Fund (HKU7062/13P) for the financial support for this study. Nobeyama Radio Observatory is a branch of the National Astronomical Observatory of Japan, National Institutes of Natural Sciences. We thank Sergey Y. Parfenov for stimulating discussions about the infrared high-dispersion spectroscopy of IRAS 19312 +1950 and the infrared sources in the surveyed region. We also thank Shuji Deguchi and Wayne Chau for their extensive help in the NRO observation.

## REFERENCES

- Afşar, M., & Bond, H. E. 2007, *AJ*, **133**, 387
- Aguirre, J. E., Ginsburg, A. G., Dunham, M. K., et al. 2011, *ApJS*, **192**, 4
- Barentsen, G., Farnhill, H. J., Drew, J. E., et al. 2014, *MNRAS*, **444**, 3230
- Barvainis, R., & Clemens, D. P. 1984, *AJ*, **89**, 1833
- Busso, M., Gallino, R., & Wasserburg, G. J. 1999, *ARA&A*, **37**, 239
- Cernicharo, J., Guelin, M., & Kahane, C. 2000, *A&AS*, **142**, 181
- Charnley, S. B., & Latter, W. B. 1997, *MNRAS*, **287**, 538
- Cooper, H. D. B., Lumsden, S. L., & Oudmaijer, R. D. 2013, *MNRAS*, **430**, 1125
- Crowther, P. A., Schnurr, O., Hirschi, R., et al. 2010, *MNRAS*, **408**, 731
- Csengeri, T., Urquhart, J. S., Schuller, F., et al. 2014, *A&A*, **565**, A75
- Cutri, R. M., Skrutskie, M. F., van Dyk, S., et al. 2003, *yCat*, **2246**, 0
- Cutri, R. M., Wright, E. L., Conrow, T., et al. 2012, *yCat*, **2311**, 0
- Damineli Neto, A., Viotti, R., Baratta, G. B., & de Araujo, F. X. 1993, *A&A*, **268**, 183
- Davies, B., Figer, D. F., Kudritzki, R.-P., et al. 2007, *ApJ*, **671**, 781
- Davies, B., Figer, D. F., Law, C. J., et al. 2008, *ApJ*, **676**, 1016
- Decin, L., Cox, N. L. J., Royer, P., et al. 2012, *A&A*, **548**, A113
- Deguchi, S., Matsunaga, N., & Fukushi, H. 2005, *PASJ*, **57**, L25
- Deguchi, S., Nakashima, J., & Takano, S. 2004, *PASJ*, **56**, 1083
- Deguchi, S., Nakashima, J., Zhang, Y., et al. 2010, *PASJ*, **62**, 391
- Deguchi, S., Imai, H., Fujii, T., et al. 2004, *PASJ*, **56**, 261
- Dunham, M. K., Rosolowsky, E., Evans, N. J., II, Cyganowski, C., & Urquhart, J. S. 2011, *ApJ*, **741**, 110
- Egan, M. P., Price, S. D., Kraemer, K. E., et al. 2003, The Midcourse Space Experiment Point Source Catalog v2.3, Air Research Laboratory Tech. Rep. AFRL-VS-TR-2003-1589
- Emerson, D. T., & Graeve, R. 1988, *A&A*, **190**, 353
- Fok, T. K. T., Nakashima, J., Yung, B. H. K., Hsia, C.-H., & Deguchi, S. 2012, *ApJ*, **760**, 65
- Frerking, M. A., Langer, W. D., & Wilson, R. W. 1982, *ApJ*, **262**, 590
- Genzel, R., Downes, D., Schwartz, P. R., et al. 1980, *ApJ*, **239**, 519
- Gomez, J. F., Uscanga, L., Suarez, O., Rizzo, J. R., & de Gregorio-Monsalvo, I. 2014, *RMxAA*, **50**, 137
- Groenewegen, M. A. T., Sloan, G. C., Soszynski, I., & Peterson, E. A. 2009, *A&A*, **506**, 1277
- Guarnieri, M. D., Renzini, A., & Ortolani, S. 1997, *ApJL*, **477**, L21
- Gvaramadze, V. V., Kniazev, A. Y., Chene, A.-N., & Schnurr, O. 2013, *MNRAS*, **430**, L20
- Habing, H. J. 1996, *A&ARv*, **7**, 97
- Hasegawa, T., Morita, K., Okumura, S., et al. 1986, in Proc. Meeting at Haystack Observatory, Masers, Molecules and Mass Outflows in Star Forming Regions, ed. A. D. Haschick (Westford, MA: Haystack Obs.), 275
- He, J. H., Dinh-V-Trung, Kwok, S., et al. 2008, *ApJS*, **177**, 275
- Hildebrand, R. H. 1983, *QJRAS*, **24**, 267
- Hsia, C.-H., Kwok, S., Zhang, Y., Koning, N., & Volk, K. 2010, *ApJ*, **725**, 173
- Hsia, C.-H., & Zhang, Y. 2014, *A&A*, **563**, A63
- Imai, H., Obara, K., Diamond, P. J., Omodaka, T., & Sasao, T. 2002a, *Natur*, **417**, 829
- Imai, H., Tafuya, D., Honma, M., Hirota, T., & Miyaji, T. 2011, *PASJ*, **63**, 81
- Imai, H., Deguchi, S., Fujii, T., et al. 2002b, *PASJ*, **54**, L19
- Ishihara, D., Onaka, T., Kataza, H., et al. 2010, *A&A*, **514**, A1
- Jamson, J. M., Rathborne, J. M., Shah, R. Y., et al. 2006, *ApJS*, **163**, 145
- Jamet, L., Perez, E., Cervino, M., et al. 2004, *A&A*, **426**, 399
- Jewell, P. R., Batrla, W., Walmsley, C. M., & Wilson, T. L. 1984, *A&A*, **130**, L1
- Jorissen, A., Mayer, A., van Eck, S., et al. 2011, *A&A*, **532**, A135
- Kaminski, T. 2008, *A&A*, **482**, 803
- Kaminski, T., Miller, M., & Tylenda, R. 2007, *A&A*, **475**, 569
- Kawada, M., Baba, H., Barthel, P. D., et al. 2007, *PASJ*, **59**, S389
- Kawaguchi, K., Kasai, Y., Ishikawa, S., & Kaifu, N. 1995, *PASJ*, **47**, 853
- Langer, W. D., & Penzias, A. A. 1990, *ApJ*, **357**, 477
- Levesque, E. M. 2009, in ASP Conf. Ser. 425, Hot and Cool: Bridging Gaps in Massive Star Evolution, ed. C. Lietherer et al. (San Francisco, CA: ASP), 103
- Lovas, F. J. 1992, *JPCRD*, **21**, 181
- Lumsden, S. L., Hoare, M. G., Urquhart, J. S., et al. 2013, *ApJS*, **208**, 11
- Maciell, W. J., Costa, R. D. D., & Idiart, T. E. P. 2011, in ASP Conf. Ser. 445, Why Galaxies Care About AGB Stars II: Shining Examples and Common Inhabitants, ed. F. Kerschbaum, T. Lebzelter, & R. F. Wing (San Francisco, CA: ASP), 343
- Martin, D. C., Seibert, M., Neil, J. D., et al. 2007, *Natur*, **448**, 780
- Mathis, J. S. 1990, *ARA&A*, **28**, 37
- Moshir, M., Kopman, G., & Conrow, T. A. O. (ed.) 1992, IRAS Faint Source Survey, Explanatory Supplement Version 2
- Mottram, J. C., Hoare, M. G., Lumsden, S. L., et al. 2010, *A&A*, **510**, A89
- Murakawa, K., Nakashima, J., Ohnaka, K., & Deguchi, S. 2007, *A&A*, **470**, 957
- Nakashima, J., & Deguchi, S. 2000, *PASJ*, **52**, L43
- Nakashima, J., & Deguchi, S. 2004, *ApJL*, **610**, L41
- Nakashima, J., & Deguchi, S. 2005, *ApJ*, **633**, 282
- Nakashima, J., & Deguchi, S. 2006, *ApJL*, **647**, L139
- Nakashima, J., & Deguchi, S. 2007, *ApJ*, **669**, 446
- Nakashima, J., Deguchi, S., Imai, H., Kembal, A., & Lewis, B. M. 2011, *ApJ*, **728**, 76
- Nakashima, J., Deguchi, S., & Kuno, N. 2004, *PASJ*, **56**, 193
- Nakashima, J., Jiang, B. W., Deguchi, S., Sadakane, K., & Nakada, Y. 2000, *PASJ*, **52**, 275
- Nakashima, J., Sobolev, A. M., Salii, S., et al. 2015, *PASJ*, **67**, 95
- Okamoto, Y. K., Kataza, H., Yamashita, T., et al. 2003, *ApJ*, **584**, 368
- Olszewski, E. W., Suntzeff, N. B., & Mateo, M. 1996, *ARA&A*, **34**, 511
- Planck Collaboration XXVIII 2014, *A&A*, **571**, A28
- Reyniers, M., & Van Winckel, H. 2001, *A&A*, **365**, 465
- Rohlfs, K., & Wilson, T. L. 2004, Tools of Radio Astronomy (Berlin: Springer)
- Rosolowsky, E., Dunham, M. K., Ginsburg, A., et al. 2010, *ApJS*, **188**, 123
- Sault, R. J., Teuben, P. J., & Wright, M. C. H. 1995, in ASP Conf. Ser. 77, Astronomical Data Analysis Software and Systems IV, ed. R. A. Shaw, H. E. Payne, & J. J. E. Hayes (San Francisco, CA: ASP), 433
- Sawada, T., Ikeda, N., Sunada, K., et al. 2008, *PASJ*, **60**, 445
- Schlafly, E. F., & Finkbeiner, D. P. 2011, *ApJ*, **737**, 103
- Schlegel, D. J., Finkbeiner, D. P., & Davis, M. 1998, *ApJ*, **500**, 525
- Scoville, N. Z., Sargent, A. I., Sanders, D. B., et al. 1986, *ApJ*, **303**, 416
- Seward, F. D., Forman, W. R., Giacconi, R., et al. 1979, *ApJL*, **234**, L55
- Shinnaga, H., Claussen, M. J., Lim, J., Trung, D. V., & Tsuboi, M. 2003, *ASSL*, **283**, 393
- Shirley, Y. L., Ellsworth-Bowers, T. P., Svoboda, B., et al. 2013, *ApJS*, **209**, 2
- Simon, R., Jackson, J. M., Clemens, D. P., Bania, T. M., & Heyer, M. H. 2001, *ApJ*, **551**, 747
- Soker, N., & Tylenda, R. 2007, in ASP Conf. Ser. 363, The Nature of V838 Mon and its Light Echo, ed. Romano, L. M. Corradi & U. Munari (San Francisco, CA: ASP), 280
- Sorai, K., Sunada, K., Okumura, S. K., et al. 2000, Proc. SPIE, **4015**, 86
- Stead, J. J., & Hoare, M. G. 2009, *MNRAS*, **400**, 731
- Straižys, V., & Laugalys, V. 2007, *BaltA*, **16**, 327
- Sunada, K., Yamaguchi, C., Nakai, N., et al. 2000, Proc. SPIE, **4015**, 237
- Szymczak, M., Hrynek, G., & Kus, A. J. 2000, *A&AS*, **143**, 269
- Townsend, L. K., Broos, P. S., Feigelson, E. D., Garmire, G. P., & Getman, K. V. 2006, *AJ*, **131**, 2164
- Ueta, T., Speck, A. K., Stencel, R. E., et al. 2006, *ApJL*, **648**, L39
- van Winckel, H. 2003, *ARA&A*, **41**, 391
- Vink, J. S., Bestenlehner, J. M., Grafener, G., de Koter, A., & Langer, N. 2012, ASP Conference Series, **465**, 207
- Walborn, N. R., Long, K. S., Lennon, D. J., & Kudritzki, R.-P. 1995, *ApJL*, **454**, L27
- Whitlock, P., & Marang, F. 2001, *MNRAS*, **323**, L13
- Wienen, M., Wyrowski, F., Schuller, F., et al. 2012, *A&A*, **544**, A146
- Wilkin, F. P. 1996, *ApJL*, **459**, L31
- Wood, P. R., Bessel, M. S., & Fox, M. W. 1983, *ApJ*, **272**, 99
- Yamaguchi, C., Sunada, K., Iizuka, Y., Iwashita, H., & Noguchi, T. 2000, Proc. SPIE, **4015**, 614
- Yung, B. H. K., Nakashima, J., & Henkel, C. 2014, *ApJ*, **794**, 81
- Yung, B. H. K., Nakashima, J., Imai, H., et al. 2011, *ApJ*, **741**, 94
- Yung, B. H. K., Nakashima, J., Imai, H., et al. 2013, *ApJ*, **769**, 20
- Zhang, Y., Hsia, C.-H., & Kwok, S. 2012, *ApJ*, **745**, 59